Hydrothermally Grown Uniform Sized Nickel Hydroxide/Oxyhydroxide Hexagonal Nanoprisms Exhibiting Room Temperature Ethanol Sensing Properties

Punam Tiwary,[a,b] *Nilanjan Chakrabarty,*[a] *Holly J. Edwards*[c], *Vinod R. Dhanak*[c], *Abhijit Kar*[d], *Rajat Mahapatra*[b,] *Amit K. Chakraborty,*[a,e]*

[a]*Centre of Excellence in Advanced Materials, National Institute of Technology, Durgapur 713209, West Bengal, India*

[b]*Department of Electronics& Communication Engineering, National Institute of Technology, Durgapur 713209, West Bengal, India*

[c]*Department of Physics, and Stephenson Institute for Renewable Energy, University of Liverpool, Liverpool, L69 3BX*

[d]*JB Centre of Excellence, Jagadis Bose National Science Talent Search, 1300 Rajdanga Main Road, Kasba, Kolkata 700107*

[e]*Carbon Nanotechnology Lab, Department of Physics, National Institute of Technology, Durgapur 713209, West Bengal, India*

*Email of the corresponding author: amit.chakraborty@phy.nitdgp.ac.in

Abstract: This work reports a simple hydrothermal method for the synthesis of uniform sized hexagonal nanoprisms (~38 nm) of β-nickel hydroxide/oxyhydroxide that show room temperature ethanol sensing properties. The films made of these nanoprisms show response as high as 120 against 100 ppm ethanol vapour at room temperature with good repeatability over several cycles and fast response and recovery times of 2s and 17s, respectively. The films of nanoprisms also show high selectivity to ethanol vapour as evident from their almost negligible responses to other alcohol vapors and non-alcoholic vapors tested in this work. What is unique about the material is that it shows no degradation in performance with aging and humidity; rather shows an improved response and selectivity to ethanol at 75% relative humidity. The enhanced performance is explained in terms of the special surface properties of the nanoprisms that can adsorb excess oxygen via oxyhydroxide formation and large surface area as confirmed by photoemission and surface adsorption studies. Further, the change in infrared absorption intensity is measured to understand the decomposition reaction of ethanol on the nanoprism surface. Thus, the synthesized material shows enormous promise as a low-cost material for room temperature ethanol sensing.

Keywords: Ethanol sensor; nickel hydroxide; hexagonal nanoprisms; photoelectron spectroscopy; humid air; room temperature;

1. Introduction:

Volatile organic compounds (VOCs) are mostly hydrocarbons released in atmosphere from sources such as furniture, buildings, food and chemical industries. Some of these VOCs have been suggested in the literature as pollutant to the environment as inhaling these VOCs above a threshold concentration can pose threat to human and animal health [1-2]. Consequently, their detection at low concentration level is very important for both human health and environmental air monitoring. In humans, alterations of metabolic pathways are sometimes associated with the production of various VOCs such as acetone, ethanol, isopropanol, 2-butanone, benzene, toluene, hexane, isoprene, etc. [3-4].These VOCs are eventually released from the body through body fluids such as exhaled breath, urine, saliva, blood, etc. Precise measurement of the concentrations of these VOCs present in these body fluids thus offers a viable method for human health monitoring. In particular, consumption/inhaling of excess ethanol, a low molecular weight VOC, has been suggested to have serious harmful effects in human health [2]. Ethanol has also been identified as a biomarker for early diagnosis of diabetes in humans [4].Detection of ethanol is of enormous interest to traffic safety as one of the main reasons of road accidents across the world is due to drunk driving which can be prevented by analyzing the exhaled breath of the drivers who have consumed beverages containing ethanol [5].Thus, detection of ethanol in human breath is not only important for the health and safety of the individual, but also for the safety of people on the road. Ethanol monitoring is also of interest to various fermentation, food and chemical industries.[6,7] Thus, it is evident that identification and detection of ethanol is of utmost importance not only for human health monitoring but also for control of indoor air pollution both at home and workplace, as well as for food and chemical industries [1-7].

However, the most commonly used analytical techniques for detection of VOCs are Gas Chromatography (GC) and GCMS (GC-mass spectrometry), which are expensive and bulky methods and suffers from cost and portability issues. Other methods of VOC sensing rely on surface acoustic waves, quartz crystal microbalance, capacitance, resistance, etc. some of which overcome the portability or cost issues but suffer from low sensitivity, selectivity, reproducibility, etc. Thus, there is an increasing demand for low-cost and portable ethanol sensors with high sensitivity (especially in humid air), and long durability.Chemiresistive

sensors, in which a sensing material (usually thin film of a metal oxide semiconductor (MOS)) shows large change in its resistance when exposed to a given VOC/gas, have gained enormous popularity as VOC and gas sensor in recent years due to its design simplicity, low cost and good chemical and thermal stability [8-10]. Till date numerous metal oxide semiconductors (MOS) [11-18] have been studied extensively for the detection of various gases and VOCs such as ethanol, methanol, acetone, formaldehyde, etc. However, most of the metal oxide-based ethanol sensors have been reported to operate at high temperatures (generally above 100°C) [17-30] which put a restriction in their use. Poor stability against aging and poor sensitivity in humid air are other issues that limit the practical use of most of these sensors [15,17-18]. Only a limited number of reports demonstrated metal oxide based ethanol sensors to work at room temperature. [30-36] For example, using zinc oxide, Shankar et al demonstrated a room temperature ethanol sensor with high sensitivity [33,34]. Recently, our group also demonstrated a room temperature ethanol sensor using ZnO nanoflowers. [35, 36] However, the selectivity, and longtime durability of these sensors were not satisfactory. Another major drawback of MOS sensors is that their sensitivity is strongly reduced in humid air which needs attention.

Nickel oxide is a well-studied oxide for sensor and other applications, [20-22,37-42] but its sensing application suffers due to high operating temperature and influence of humidity. On the contrary, nickel hydroxide which often serves as the precursor for producing the oxide, has not been sufficiently explored as VOC sensor, although it showed huge potential for its energy storage application [43-44]. A few groups claimed to have used $Ni(OH)_2$ for sensing of gases, but when we read these, we found that the sensing was performed by NiO, since their operating temperature was 300°C [45-47].It is therefore, evident that there is a need for research for development of VOC sensors using nickel hydroxide and especially for room temperature ethanol sensor which nickel oxide based sensors cannot exhibit. The β-phase of $Ni(OH)_2$ is isostructural with brucite $Mg(OH)_2$ structure and occurs naturally as the mineral theophrastite [48,49] which is very stable and thus may fulfil our expectation of high durability in humid environment.

In view of the above, herein, we report the synthesis of $Ni(OH)_2$ using a facile hydrothermal method with an aim to evaluate its sensing performance against VOCs. X ray diffraction (XRD) and scanning electron microscopy (SEM) analyses were conducted to evaluate the morphology and microstructures of the synthesized materials which revealed the formation of

uniformly sized (38 nm) hexagonal nanoprisms of crystalline β-$Ni(OH)_2$ (NHNP). XPS was employed for identification of elemental composition and chemical states of these NHNP whereas the surface area was estimated by N_2 sorption isotherms. Thin films made of the synthesized NHNP were then exposed separately to the vapour of a number of VOCs to test their sensing response at room temperature against each of these VOCs. The dynamic response-recovery curves were recorded at different ethanol exposures (both in dry and humid air) and the corresponding sensor response, and response-recovery times were estimated. The stability of the sensor was evaluated over a period of six months and the sensing mechanism was explained based on formation of space charge layer on NHNP surface. Fourier transform infrared (FTIR) spectroscopy was used to investigate the chemical reaction of ethanol with pre-adsorbed O_2^-ions on NHNP surface by measuring the quantity of CO_2 signal evolved during exposure of the NHNP sensor to ethanol.

2. Experimental

2.1 Synthesis of NHNP

The details of the synthesis of the NHNP were reported in our previous publications [43-44]. In brief, it involved as first step, the mixing of aqueous solutions of 0.1 M $Ni(NO_3)_2.6H_2O$ (1.16 gm) and 1M NaOH (1.6 gm) under continuous stirring at 500 rpm. After stirring for a further 30 min, the resulting solution was transferred to a 100 mL Teflon lined stainless steel autoclave and kept at 140 °C for 12 h followed by a natural cooling to room temperature. The reaction mixture was subsequently washed with DI water until pH 7 and filtered followed by a further wash with ethanol to remove any unreacted precursors. The final product was obtained as a powder of $Ni(OH)_2$ after drying the filtrate under an infrared lamp.

2.2 Material Characterization:

The crystallinity of the synthesized material was investigated by powder X-ray diffraction method (PANALYTICAL X Pert Pro) using Cu Kα radiation (1.54Å). The surface microstructure and morphology was analysed by a field emission scanning electron microscope (FESEM) (Carl-Zeiss Sigma) operated at 10 kV accelerating voltage and the sample in powder form was pressed on a carbon tape for imaging. Further analyses of the FESEM micrographs were carried out using ImageJ software. Chemical analysis of the nanoparticles was conducted by X-ray photoelectron spectroscopy (XPS) using an Al Kα source (1486.6 eV) and an electron energy analyser (PSP Vacuum Technology) in normal emission geometry. The samples for XPS were prepared by drop casting a slurry of $Ni(OH)_2$

on a Si(100) substrate. The binding energies were corrected by setting the position of the C1s peak originating from adventitious carbon at 284.7 eV in accordance with established literature [50-51]. The XPS data were analysed using CasaXPS software, the peaks were fitted with Gaussian/Lorentzian line shapes and the background was fitted with a Shirley type background subtraction. Attenuated total reflectance (ATR) spectra for infrared light were obtained using a Shimadzu IR Affinity-1S FTIR Spectrometer equipped with a diamond ATR attachment in the spectral range of 400 cm^{-1} to 4000 cm^{-1} with resolution of 8 cm^{-1}.

2.3 Fabrication of the sensor

The sensors were fabricated by drop-casting a slurry of NHNP in ethanol (2.5 mg/ml) on clean glass slides followed by drying in a vacuum desiccator for 12 h. The thickness of the $Ni(OH)_2$ thin film on the glass substrate was estimated from the cross-sectional FESEM images. The sensor (i.e., NHNP coated glass) was then mounted in the sensing chamber to which four crocodile clips were connected to a source meter (Keithley 2450) through an electrical feed-through. The source meter was interfaced with a computer for data recording. For our electrical measurements, two probes were shorted on each side in order to take only two probe measurements. The schematic of the indigenously designed gas sensing chamber and the electrical measurements is presented in figure 1.

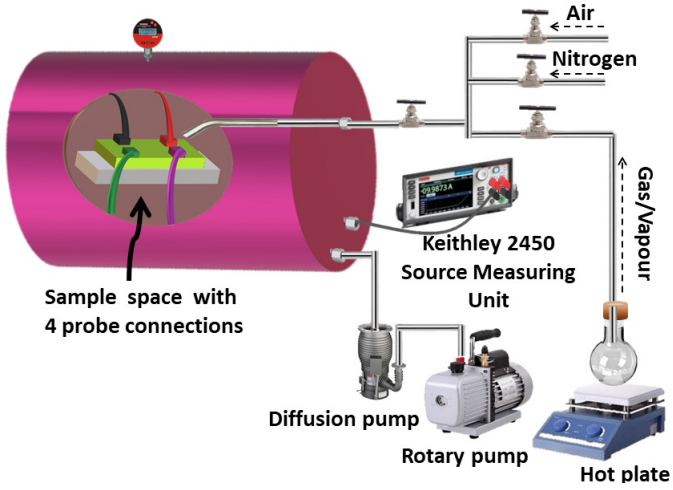

Figure 1: Schematic of the Sensor measurement set up.

As it can be observed from figure 1, the indigenous gas sensing set-up consists of three inlets connected to nitrogen, air and the test gas/VOC vapour. To ensure that the analyte vapour/gas flows into the sensing chamber (where the sensing device is mounted using a sample holder), it is pre-evacuated by a diffusion pump (backed by a rotary pump).

For ethanol sensing, appropriate volume of liquid ethanol was taken in a glass vessel whose mouth was connected to one of the gas inlets going into the sensing chamber. Gentle heating was provided to this vessel which together with low pressure of the sample chamber, achieved by its pre-evacuation, causes the ethanol vapour to easily flow into the chamber. Recovery of the sensors was achieved by pumping out the chamber (i.e. the VOCs) once the electrical resistance of the sensor film reached its highest value for a given ethanol exposure. The concentration (C) of ethanol vapour (ppm) was estimated using the following equation.

$$C = \frac{V_e}{V_c} \times 10^6 \quad (1)$$

Where, V_e and $V_c$are the volumes of the liquid ethanol and the sample chamber, respectively. The response (S) of the sensor was defined by the ratio of the electrical resistance of the $Ni(OH)_2$ film in absence of any gases to that in ethanol vapour and is given by,

$$S = \frac{R_a}{R_g} \quad (2)$$

where, R_a and R_g are the electrical resistances of the sensor in absence of the analyte (ethanol) and in presence of it, respectively. The response and recovery times were defined by the times required to reach 90% of the total resistance variation when ethanol vapour was flown in and out, respectively.

3. RESULTS & DISCUSSIONS

3.1 Structural and morphological analysis

The X- ray diffraction (XRD) pattern of NHNP is presented in figure 2(a) which shows peaks corresponding to (001), (100), (011), (012), (110), (111), (200), (103), (201), (202) and (113) planes of crystalline β phase of $Ni(OH)_2$ in accordance with AMCSD file no. 001803. The average crystallite size (D) of NHNP was estimated to be 23 nm from the most intense peak of (001) plane using Debye-Scherrer formula given by,

$$D = \frac{k\lambda}{\beta cos\theta} \quad (3)$$

where k =0.9, λ=1.5418 Å, β is the full width at half maximum (FWHM) of the (001) peak and θ is the corresponding diffraction angle.

Figure 2(b) presents an FESEM micrograph of the NHNP powder which reveals hexagonal prism shaped particles of uniform size and shape. A hexagonal shape particle is identified and expanded within the image of Fig. 2(b) as inset. Analysis of the size of the particles using ImageJ and the subsequent histogram plot of the size distribution is shown in Figure 2(c)

where one can see that the size of the NHNP varied between 30 and 60 nm with a mean value of 38 nm. In order to estimate the thickness of the $Ni(OH)_2$ film, i.e. the sensing film, cross-sectional image of the film was recorded using the FESEM as shown in Figure 2 (d) where one can see that the typical thickness of the film is ~570 nm.

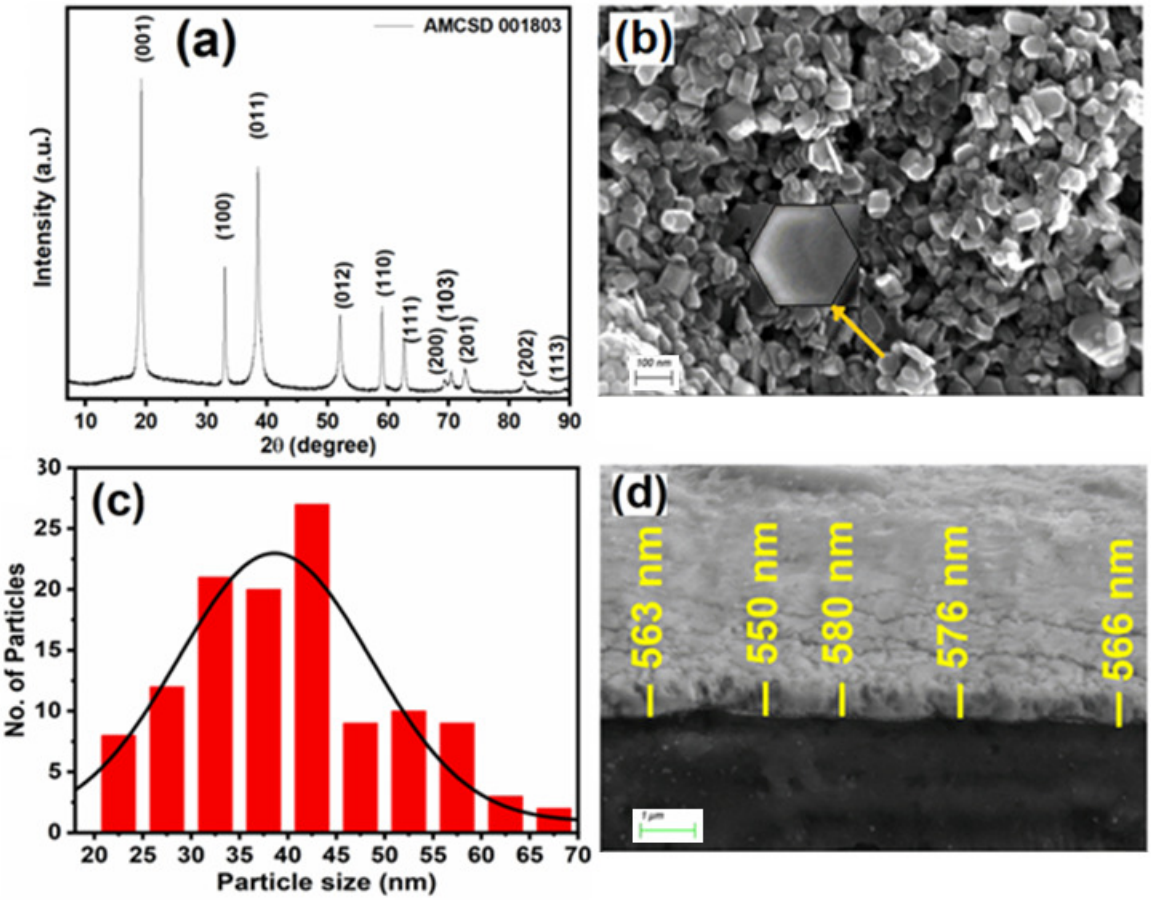

Figure 2: (a) XRD pattern (b) FESEM image of NHNP powdered film. (c) Histogram plot showing particle size distribution of NHNP and (d) Cross-sectional FESEM image of the NHNP on glass substrate.

3.2 Surface Chemical Analysis of NHNP

The survey XPS spectrum (Fig. 3(a)) obtained from the NHNP film revealed the presence of elements like nickel, oxygen, silicon and carbon of which Si originates from the substrate on which $Ni(OH)_2$ was coated possibly due to pinholes within the film and carbon originates from the atmospheric contamination (adventitious). Absence of signals of any other elements confirms the cleanliness of the $Ni(OH)_2$ film. The atomic composition was calculated from the XPS data by evaluating the areas under the core-level spectra of Ni $2p_{3/2}$, O1s, C 1s, Si 2p, and taking into account the respective sensitivity factors [52]. This analysis revealed the presence of 7.69 at.% Ni, 69.49 at.% O, 10.18 at. % C, and 12.64 at.% Si. A closer inspection

further reveals that out of 69.49% oxygen, Si and Ni together account for about 40%, (assuming Si is present as SiO_2), thus suggesting the presence of almost 30 at.% (about 43% of total oxygen) non-stoichiometric oxygen originating from the pre-adsorbed oxygen species on the NHNP surface from atmospheric exposure.

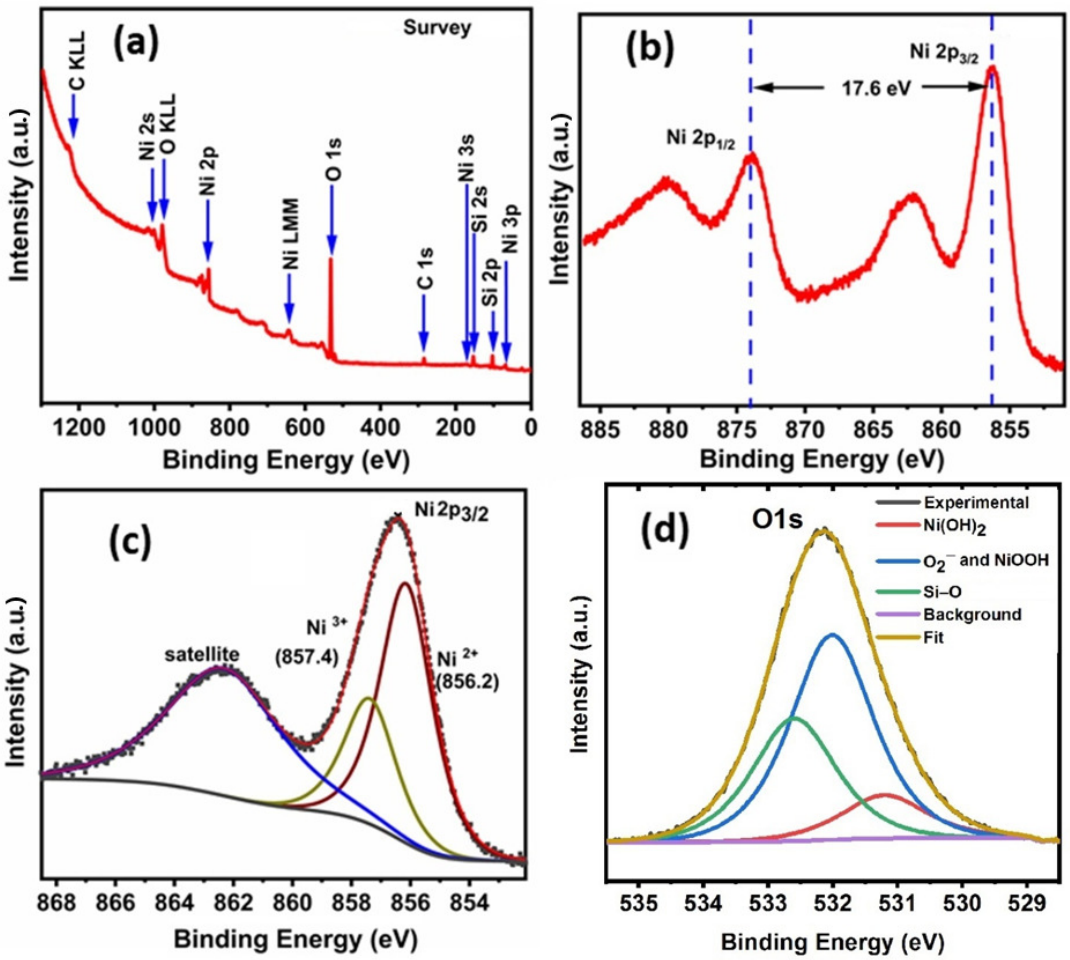

Figure 3: XPS plots of NHNP - (a) Survey, (b) Ni 2p extended spectrum. (c) Ni $2p_{3/2}$ and (d) O 1s spectra decomposed into various components.

Ni 2p spectrum (Fig.3(b)) shows presence of two most intense peaks centred around 856.4 eV and 874.0 eV separated by 17.6 eV corresponding to photoelectrons emitted from Ni $2p_{3/2}$ and Ni $2p_{1/2}$ orbitals in accordance with the formation of a mixed β-NiOOH and $Ni(OH)_2$ [53-54]. Additional pair of satellite peaks observed at binding energies of about 5.5 eV higher than the above two main peaks originate from the half-filled d-orbital of Ni which causes a continuous transition of electrons from d to p orbitals and is commonly observed in Ni based compounds [54-55]. To identify the detail chemical state of nickel in NHNP, Ni $2p_{3/2}$ spectrum was deconvoluted into components by curve fitting (Fig. 3(c)) which shows

existence of two strong components at 856.2 eV and 857.4 eV, corresponding to Ni^{2+} and Ni^{3+} states in accordance with the formation of $Ni(OH)_2$ and NiOOH phases, respectively[55]. Quantitative analysis of the components revealed that of the total Ni metal, about 67.4 at. % Ni is present in the sample as $Ni(OH)_2$ whereas the rest is NiOOH.

The deconvoluted O1s spectra is presented in figure 3 (d) which has been obtained by maintaining similar FWHM values using CASAXPS. Three components were enough to get a good fit of the data as shown in 3(d).The component peaking at 531.2 eV is due to lattice oxygen, i.e., oxygen bound within $Ni(OH)_2$[55] whereas the component peaking at 532.6 eV is likely to be associated with oxygen bound within SiO_2 substrate. The most interesting component is the one in the middle peaking at 532.0 eV which has the highest intensity encompassing nearly 55% of the total oxygen signal. This component originates from the surface adsorbed oxygen (O_2^-) species [56,57] which is in good agreement with the expected 43 at% non-stoichiometric oxygen as discussed above. The slightly higher intensity of 55% is possibly because this component also encompass the oxygen signal (about 5 at%) due to NiOOH since its binding energy is also around 532.1 eV as assigned in the established literature[55]. The fitting also revealed that about 12 % oxygen signal is due to $Ni(OH)_2$ whereas the remaining 33% is due to oxygen bound to SiO_2 substrate both of which are in good agreement with the expected atomic percentages of Ni and Si as discussed above.

3.3 Evaluation of the NHNP film as Sensor

3.3.1 In moisture free (dry N_2) atmosphere:

Figure 4 (a) shows the resistance transients of the sensor at different concentrations of ethanol in the range of 50-150 ppm where one can clearly see that a sharp decrease in the resistance occurs as soon as the sensor is exposed to ethanol vapour which soon saturates to a minimum value at each ethanol concentration. It can be further observed that the saturation (lowest) resistance of the sensor monotonously decreased with increase in the ethanol concentration (ppm) although the rate slowed down above 125 ppm and almost saturated at 150 ppm. In terms of response, the sensor showed its highest responses of 180 and 120 against 150 and 100 ppm of ethanol exposure, respectively which is remarkable. The slowing down of the rate of decrease of saturation resistance can be understood by considering that above 150 ppm, number of ethanol molecules are high enough to use up all the available molecules of NHNP film so that a further increase in ethanol has no impact on the sensor resistance. The lowest concentration of ethanol measured by the NHNP sensor was 25 ppm at which the sensor

showed a very low but detectable response of 1.4 in dry air and 1.7 in 75% RH (not shown) which could be understood by considering that the actual ethanol concentration could be much less than that measured by us because part of the ethanol could be trapped on the inner walls of the long (~2 feet) and narrow (6 mm diameter) pipes and large sensing chamber (6.75 L) and could remain unaccounted for. Since the number of such unaccounted (lost) ethanol molecules does not increase after it saturates the walls, its influence on the estimate of concentration will be highest at low concentration and negligible at higher concentrations. This means that the actual response of the sensor at 25 ppm could be much higher if we were able to account for the lost molecules of ethanol. On the other hand, for ethanol concentration above 150 ppm, it took long time for us to degas the chamber since our sample holder was not equipped with a heater and hence we avoided taking measurements above 150 ppm.

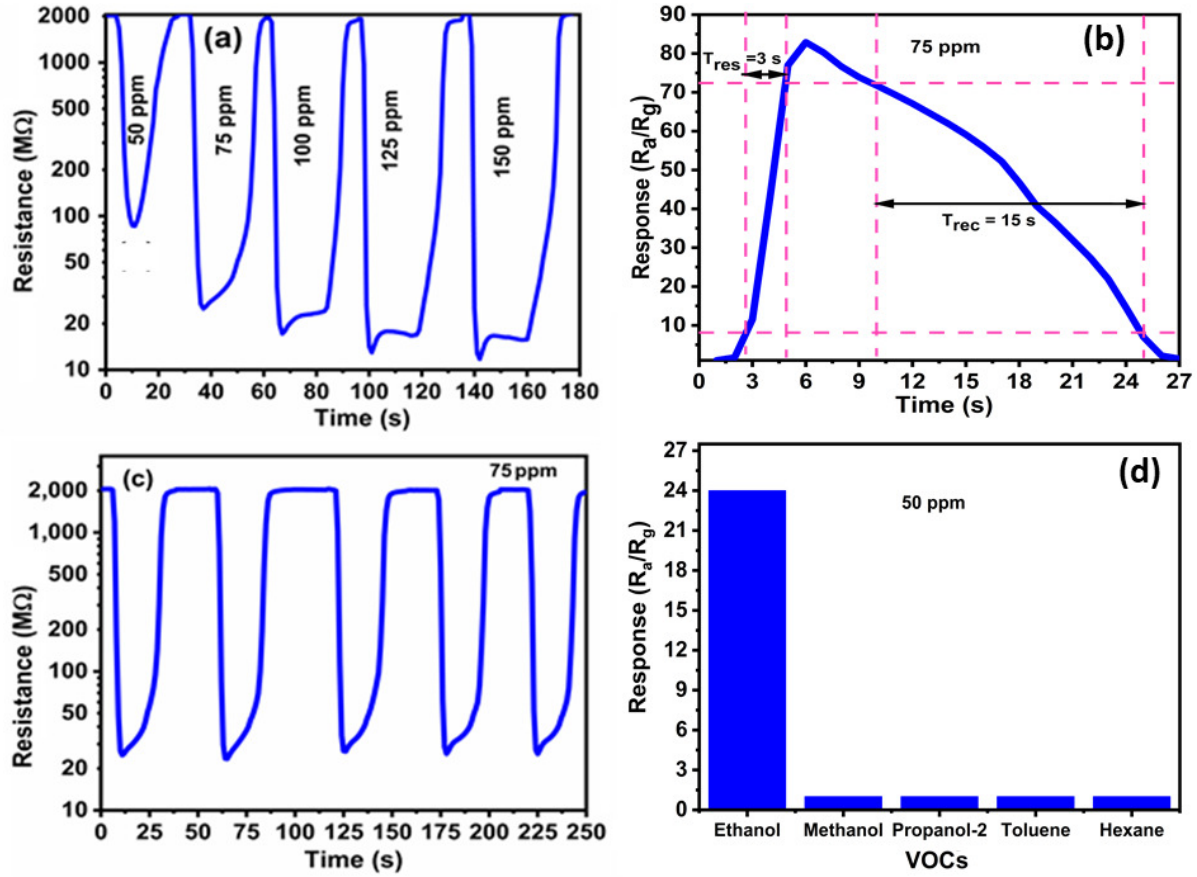

Figure 4: Performance parameters of the NHNP sensor tested in dry N_2 atmosphere at room temperature. (a) Resistance transients at different concentrations of ethanol; (b) Expanded view of the response transient at 75 ppm highlighting the response and recovery times; (c) Repeatability plot showing five consecutive cycles of transients recorded at 75 ppm ethanol exposure; (d) Highest responses against exposure to 50 ppm of different VOCs.

An expanded view of the response transient at 75 ppm is presented in Figure 4(b) demonstrating how the response and recovery times were calculated. It can be seen that the response and recovery times of the sensor are 1.8s and 4s, respectively thus indicating fast response and recovery times. The recovery process begins slowly as one can see that a flat plateau exists for about 20s before the recovery starts essentially because we did not supply any heat to the NHNP film after reaching the saturation resistance for removal of ethanol (which is commonly used by other researchers) and instead allowed degassing through evacuation of the chamber. Figure 4(c) presents the resistance transients for five consecutive cycles against 75 ppm of ethanol which confirms that the sensor response data is very much reproducible as all the transients show identical values of base resistance and lowest (saturation) resistance. Figure 4(d) plots the highest responses of the sensor against exposure to 50 ppm of different VOCs in which one can see that the sensor has its highest response of 24 against ethanol but almost no response to other VOCs tested. At higher concentrations, the sensor exhibited some response, although much less than that against ethanol, to other alcohols such as methanol and 2-propanol which is not surprising and I accordance with previous literature given the interaction of alcohols with semiconductor follows somewhat similar mechanisms (discussed later)[35,58]. The selective high response of the sensor to ethanol compared to methanol can be understood from the reactions that these two VOCs exhibit with the pre-adsorbed oxygen species on sensor surface (discussed later in Eq. 4 and Eq.5), as one can see that each ethanol molecule releases three electrons but it requires two molecules of methanol to release the same number of electrons making the response of the sensor half that for ethanol when both VOCs are used with same ppm of concentration. In addition, the hydrogen bonding within methanol is much stronger than that of ethanol making it difficult for methanol to interact with other molecules. Thus it can be safely concluded that the NHNP sensor exhibits very good selectivity to ethanol.

3.3.2 NHNP Sensor Performance in Humid Air (75% RH @ 33°c):

Since the sensor performance often degrades with presence of humidity, we have evaluated the performance of our sensor against humid air of different % RH in terms of change in resistance. Figure 5 (a) shows the resistance transients of the sensor at 50, 75,100,125 and 150 ppm concentrations of ethanol in which one can observe sharp decrease in resistance when exposed to fixed concentration of ethanol vapour followed by a gradual recovery upon removal of ethanol. Comparison of the transients recorded at different ethanol exposure levels further reveals a slow and gradual decrease in the value of the saturation (lowest)

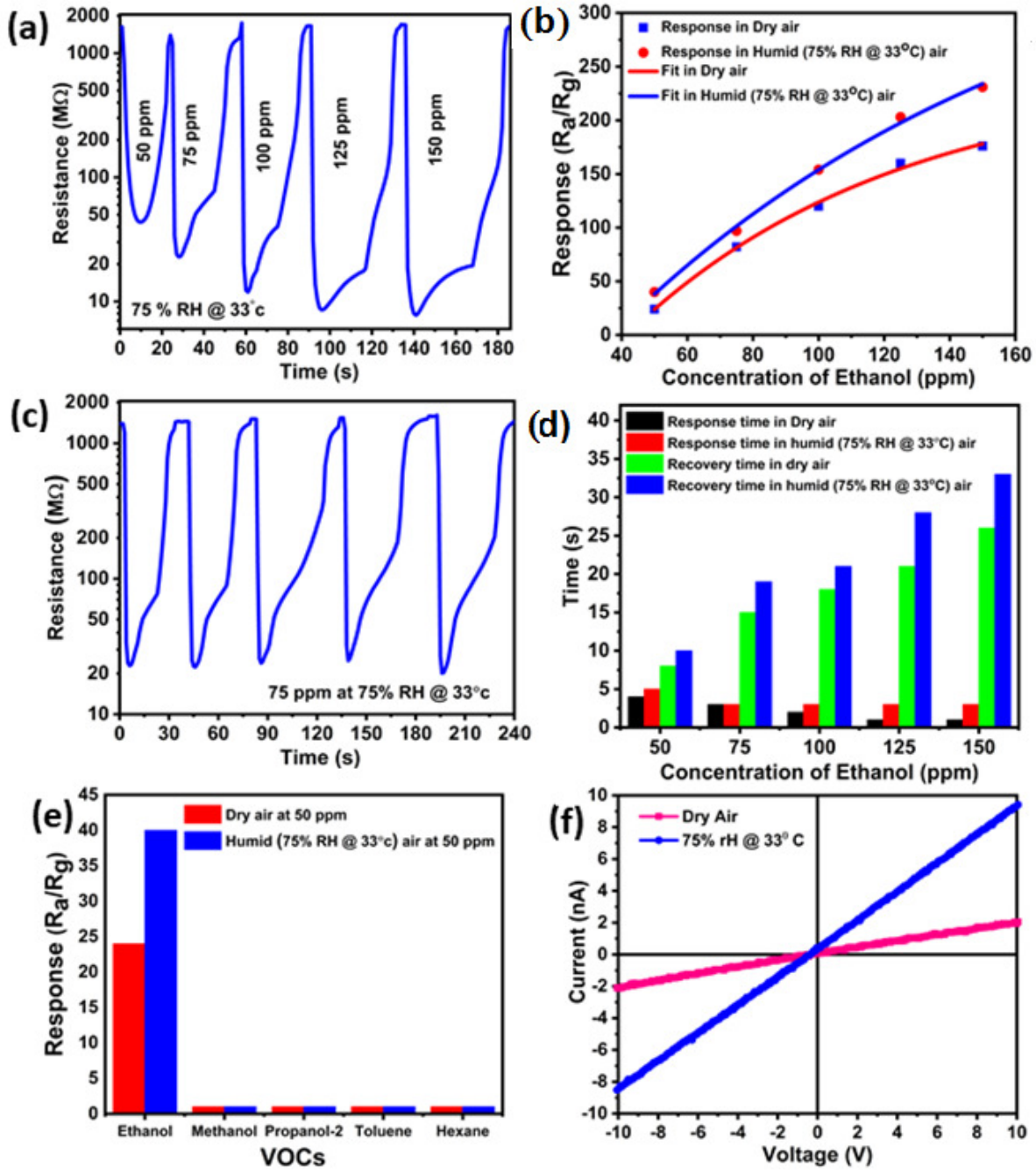

Figure 5: Performance parameters of the NHNP sensor tested at 75% RH at 33°C. (a) Resistance transients at different concentrations of ethanol; (b) Variation of highest responses against different ethanol concentrations, (c) Repeatability plot showing five consecutive cycles of transients recorded at 75 ppm ethanol exposure; (d) Highest responses against exposure to 50 ppm of different VOCs; (e) Highest responses in dry and humid (75% RH) conditions against 50 ppm of different VOCs; (f) Current – voltage characteristic (I-V plot) of the NHNP sensor.

resistance very similar to that observed in dry air. However, the magnitudes of the saturation resistance recorded against each fixed concentration of ethanol decreased from their dry air values thus increasing the overall responses of the sensor to higher than those in dry air. As a consequence, in humid air the sensor showed its highest responses of 250 and 154 against 150 and 100 ppm ethanol exposure, respectively which are much higher than those in dry air. Figure 5(b) plots the sensor response at various ethanol concentrations both in dry and humid (75% RH) air in which it is evident that the response of the sensor increases with increased ethanol concentration for both the cases. The graph also shows that the magnitudes of response are higher in humid air than in dry condition for all ethanol concentrations. With increased concentration of ethanol the response is expected to increase due to larger interaction of the semiconductor surface with incoming ethanol molecules resulting in larger reduction of the resistance of the nanoprisms.

Figure 5(c) presents the resistance transients for five consecutive cycles against 75 ppm of ethanol which confirm that the sensor response data is very much reproducible as all the transients show almost identical values of base and saturation resistances. Figure 5(d) compares the response-recovery times of the sensor at each ethanol concentration both in dry and humid air. One can see for both dry and humid conditions, that the recovery time is much larger than the response time and that the recovery time gradually rises with increase in ethanol concentration. Also to note is that in dry condition, the response time gradually reduces with increased concentration (from 4s at 50 ppm to almost 1 s at 150 ppm) but in humid condition it is more or less constant at about 4s. Thus, it is evident from the graph that the sensor responds faster but recovers slowly in humid air than in dry air which is in accordance with the difficulty of degassing of moisture. Figure 5(e) plots the response values against 50 ppm ethanol both in dry and humid (75% RH) where one can see that the sensor is highly selective to ethanol vapour as the magnitudes of responses against other VOCs tested are negligible. In fact, what is even more interesting is that the selectivity of the sensor to ethanol is more prominent in humid air (75% RH) than in dry air which is potentially very useful, especially in detecting low level of ethanol from a mixture of moist VOCs and demands for further research attention on the material. Current-voltage characteristic of the sensor both in dry and in humid (75% RH) are shown in Figure 5(f) in which the straight lines passing almost through the origin indicating the ohmic contact.

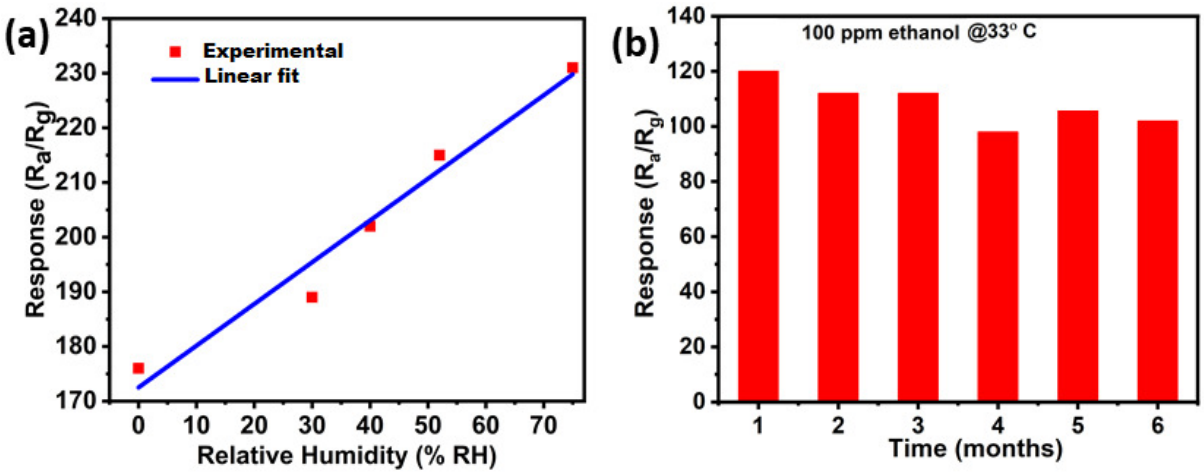

Figure 6: Highest responses of the NHNP sensor (a) against 150 ppm of ethanol as a function of %RH; and (b) against 100 ppm ethanol exposure in 75%RH at 33ºC over six months.

In order to assess the nature of dependence of the sensor response as a function of relative humidity of the air, the responses of the sensor, were recorded against our highest ethanol exposure level of 150 ppm at RH values (@ 33ºC) of 30%, 52%, 75% and 85% which are plotted in figure 6(a). The plot clearly establishes an increasing positive influence of RH on the sensor response. For this study, we chose 150 ppm concentration of ethanol to maximize the difference of responses compared to dry atmosphere. Figure 6(b) presents a plot of the highest responses of the sensor at 100 ppm ethanol exposure recorded over a duration of six months at an interval of ~one month. It is evident that the value of response did not change a lot within six month of aging time suggesting good durability of the sensor which is remarkable.

To understand why NHNP sensor performs better in humid air, we note the recent first principles calculation by Eslamibidgoli et al [59] in which the authors observed a much higher degree of ordering of surface water layers on Ni(OOH) surface compared to that of β-$Ni(OH)_2$due to large surface polarization effect on the former. This means that the presence of some surface Ni(OOH) in our sensor material is helpful in adsorbing water molecules when it is exposed to humid air. Another study by Cheng et al. [60] showed that the presence of water molecules can catalyse the reaction of ethanol with O_2^- ions. This explains why our sensor exhibits enhanced response to ethanol in humid air than in dry air. Thus, overall, from the plots in figure 4 and 5, it can be concluded that NHNP sensor performs better in humid air than dry air as its response and selectivity are both higher in humid air and it responds faster in humid air which are highly desirable for good sensor.

To explain the high selectivity of NHNP sensor to ethanol, the room temperature reactions of ethanol [32, 61], methanol [13, 62], 2-propanol [62], toluene [63] and hexane [64] are shown in the following equations (4) to (8):

$C_2H_5OH + 3O_2^- \rightarrow 2CO_2 \uparrow + 3H_2O \uparrow + 3e^-$ (ethanol) (4)

$2CH_3OH + 3O_2^- \rightarrow 2CO_2 \uparrow + 4H_2O \uparrow + 3e^-$ (methanol) (5)

$2C_3H_7OH + 9O_2^- \rightarrow 6CO_2 \uparrow + 3H_2O \uparrow + 3e^-$ (propanol-2) (6)

$C_7H_8 + 9O_2^- \rightarrow 7CO_2 \uparrow + 4H_2O \uparrow + 9e^-$ (Toluene) (7)

$C_6H_{14} + 19O_2^- \rightarrow 12CO_2 \uparrow + 14H_2O \uparrow + 19e^-$ (Hexane) (8)

The electron withdrawing effect of the OH molecule is distributed among three C-H bonds in methanol whereas in ethanol it is distributed between two α C-H bonds thus making it weaker in methanol. As a consequence, the activation energy of ethanol is lower than that of methanol. On the contrary, for 2-propanol, a secondary alcohol, both size and activation energy are higher than those of ethanol and methanol[65]. In fact, the intermediate reaction product of 2-propanol is a ketone whereas in case of primary alcohols, the intermediate product is an aldehyde which is the reason why 2-propanol has a higher activation energy. Toluene and hexane being large non-polar, they form complex intermediates requiring large activation energy and therefore, the NHNP sensor is almost insensitive to these analytes at room temperature. Thus, it is understood why the sensitivity of the NHNP sensor is the highest towards ethanol compared to other VOCs.

3.4 Sensing Mechanism:

The sensing mechanism of semiconductors against VOC is closely related to their ability to adsorb oxygen molecules on the surface [8,35,56]. Adsorption is a surface phenomenon in which molecules of a compound are accumulated at an adsorbent surface in gas or liquid form [66]. Depending upon the interaction between the molecules and the surface, adsorption can occur in two ways:

(i) physical adsorption also called “physisorption,” in which the weak forces such as electrostatic interactions and Van der Waals forces are involved and

(ii) Chemical sorption, also called “chemisorptions” in which strong chemical bonds such as covalent bonds are formed between the surface and the adsorbed molecules.

When NHNP are exposed to air, oxygen molecules are adsorbed onto its surface and these adsorbed oxygen molecules extract electrons from the conduction band (CB) of NHNP whereby forming adsorbed oxygen ions as indicated in equations (9) to (13). [13]

$O_2(\text{gas}) \leftrightarrow O_2(\text{ads})$ (9)

At temperatures below 150°C , the dominating process is,

$O_2(\text{ads}) + e^-(NHNP) \rightarrow O_2^-(\text{ads})$ (10)

At high temperatures (above 150°C), the dominating processes are,

$O_2^-(\text{ads}) \leftrightarrow 2O^-(\text{ads})$ (11)

$O^- + e^-(NHNP) \rightarrow O^{2-}(\text{ads})$ (12)

$O^{2-} \leftrightarrow O^{2-}$ (First bulk layer) (13)

Obviously, for better sensing response, the sensor (NHNP) would require more pre-adsorbed oxygen species on its surface which in the present work was facilitated by a nanostructured surface with its rough and porous design. Indeed, the surface area of the NHNP measured from their N_2 sorption isotherms (Fig. 7(a)) and by employing BET theory was found to be pretty large (72.5 m^2/g) suggesting a porous structure of the NHNP material and the average pore size, to be 18.4 nm from BJH theory (Inset in Fig. 7(a)). The adsorption isotherm of NHNP in figure 7(a) appears to be Type III referring to multilayer adsorption indicating a physical adsorption process on microporous NHNP adsorbent because a chemical adsorption usually occurs by formation of a single molecular layer (monolayer) on the adsorbent surface [66].

Due to its large surface area, when NHNP comes in contact with atmosphere, large number of oxygen species get adsorbed on its surface by extracting electrons from the CB of NHNP. This causes the formation of a thick space charge layer on the surface of NHNP films which in turn sharply increases the potential barrier yielding a much higher value of electrical resistance than actual. Upon exposure to a reducing gas molecule like ethanol vapour, the adsorbed oxygen ions react with ethanol via equation (4) [30-36,56], whereby the trapped electrons are released back to the CB of the NHNP film making it electrically more conductive which is measured as the sensor response.

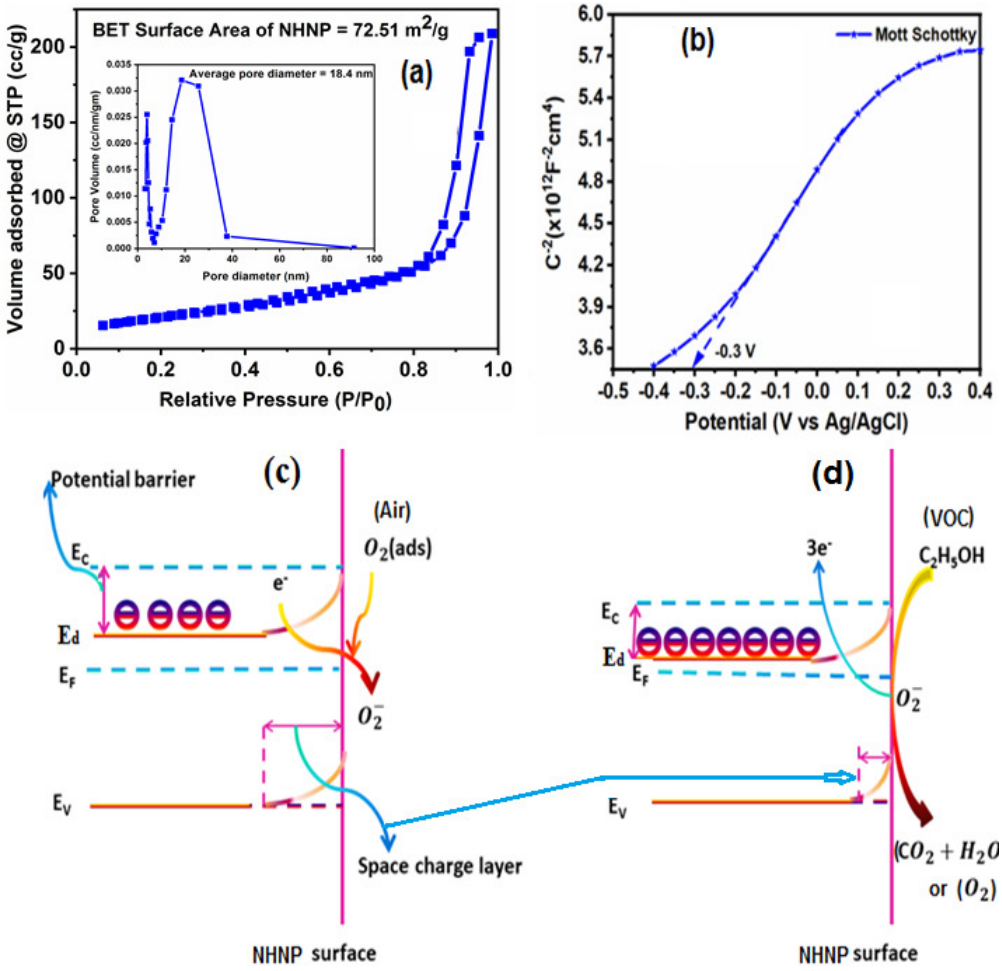

Figure 7: NHNP characteristics - (a) N_2 sorption isotherms and pore size distribution (inset), (b) Mott-Schottky plot, (c) schematic band diagram in normal atmosphere and (d) the change in the band diagram when exposed to ethanol.

To construct a schematic band diagram of the NHNP it is important to know whether it is a n-type or p-type semiconductor. In the literature there are suggestions that $Ni(OH)_2$ is a n-type semiconductor, [67] but to be sure that the NHNP synthesized in this work is also n-type, we did Mott-Schottky analysis as shown in Fig 7(b) where one can clearly see a negative slope of the plot confirming the n-type behaviour of NHNP. Fig. 7(c) plots a schematic band diagram of NHNP normally exposed to ambient atmosphere whereas Fig. 7(d) shows the same upon exposure to ethanol vapour. It is evident that the response is produced by the shrinkage of the space charge layer (from Fig. 7c to 7d) due to adsorption and reaction of ethanol molecules with pre-adsorbed O_2^-ions on the NHNP surface which results in the reduction of the electrical resistance of the NHNP along with production of CO_2 and H_2O both in the gaseous form.

To further verify this mechanism, we tried to quantify the evolved CO_2 in the above reaction by in situ monitoring of the infrared spectrum of the NHNP film as it was exposed to ethanol. In Figure 8(a), the absorbance curve of the NHNP not exposed to any VOC but exposed to air is shown in which a sharp band in the region 3300 cm^{-1} to 3700 cm^{-1}, due to OH stretching vibration of hydroxide confirms the brucite structure of β-$Ni(OH)_2$ phase [68]. The bands at 500 cm^{-1} and 435 cm^{-1} originate from Ni-OH bend and Ni-O lattice vibrations associated with $Ni(OH)_2$ [69]. The small humps in the region between 2300 and 2400 cm^{-1} are indicative of the presence of CO_2 vibrations originating from atmosphere of the sample inside the spectrometer. Any change in the intensity of this hump from sample to samples would indicate a change in the quantity of CO_2 in the atmosphere.

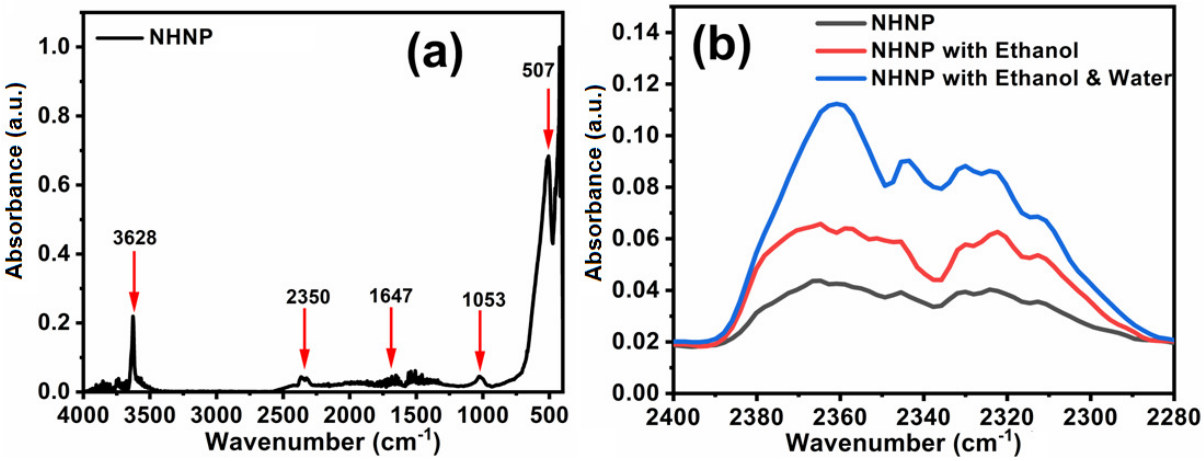

Figure 8: (a) FTIR spectrum of NHNP, (b) FTIR spectra of NHNP, NHNP exposed to ethanol and NHNP exposed to ethanol/water mixture.

In figure 8(b) the FTIR spectra obtained from NHNP at different exposure conditions are compared where one can see small humps around 2350 cm^{-1}that characterises the presence of small amount of CO_2 for samples of NHNP, water, and water/ethanol mixture in accordance with expectation. While this hump due to CO_2, for NHNP not exposed to ethanol, shows ~4% intensity, it rises to about 6% for NHNP exposed to ethanol and about 11% when exposed to a solution of equal concentration of ethanol and water. The enhancement of intensity of the CO_2 related hum for the two cases where NHNP were exposed to ethanol suggests that CO_2 was indeed produced during interaction of ethanol with NHNP. Since the highest intensity is observed for the NHNP sample exposed to ethanol and water mixture, we can further conclude that presence of water assists the reaction presented in equation (4) yielding higher amounts of CO_2. This, in turn, explains why we see a better sensor performance of the NHNP

sensor in humid air than that in dry atmosphere as discussed earlier. Thus, we have experimentally verified the products that come out during sensing of ethanol by our sensor.

Finally, to realise the importance of this work with respect to existing room temperature ethanol sensors, the performance parameters of NHNP sensors are compared with those of published reports in Table 1. It is evident that the NHNP sensor performs better than the other NiO based ethanol sensors in terms of a number of sensor parameters.

Table 1: Comparison of the performance parameters of the NHNP sensor with those of reported NiO based ethanol sensors.

Sr. no.	Sample detail	Temp. (°C)	Ethanol conc. (ppm)	Sensor Response	Response/ Recovery time (s)	Ref. no.
1	Fe doped NiO nanowires	320	100	$\frac{R_g}{R_a} = 14.30$	25/11	20
2	Coral-like $Cu_xNi_{(1-x)}O$ based resistive sensor	250	540	$\frac{R_g}{R_a} = 14.30$	NA	21
3	Ultra-thin NiOnanosheets with neck connected networks	200	500	$\frac{R_g}{R_a} = 4.5$	64/211	22
4	Sputtered NanocrystallineNiO thin films	250	5	$\frac{R_g}{R_0} = 7$	167/99	38
5	Au-functionalised NiO nanoparticles	325	1000	$100 \times \frac{R_g}{R_a}$ =4.42	~22/200	39
6	NiO nanowires calcined at 650°C	300	100	$\frac{R_g}{R_a} = 5.26$	15/49	40
7	Rose like NiO nanoparticles	230	5	$\frac{R_g}{R_a} = 8.4$	21/14	41
8	Platelet-like $Ni(OH)_2$converted to NiO at 313°C	350	100	$\frac{R_g}{R_a} = 1.85$	NA	45
9	$Ni(OH)_2$chemically converted NiO	350	100	$\frac{R_g}{R_a} = 1.8$	NA	46
10	Hexagonal nanoprisms of β-$Ni(OH)_2$	33	100	$\frac{R_a}{R_g} = 120\ (dry\ air)$ $\frac{R_a}{R_g} = 154(75\%RH)$	2/20 (dry air) 2/24 (75%RH)	This work

4. Conclusion:

In conclusion, $Ni(OH)_2$ hexagonal nanoprisms (NHNP) of uniform size (38 nm) and shape were synthesized by a facile hydrothermal method and their sensing properties against different common VOCs were tested at room temperature, both in dry and humid environment. Characterization of the NHNP using XRD, FESEM, XPS and FTIR confirmed the hexagonal nanoprism like particles made of crystalline β-$Ni(OH)_2$. Sensing experiments with NHNP showed n-type behaviour when exposed to reducing gases such as ethanol. The sensor showed its highest response of 120 and 154 against 100 ppm of ethanol in dry and humid air, respectively whereas it showed negligible responses against other VOCs tested in this work. Both selectivity and response of the sensor improved in humid air, thus showing its potential use in detecting ethanol with high sensitivity from a humid air mixture. The NHNP sensor showed fast response of 2s and recovery time of 17s, respectively against 100 ppm ethanol and it also showed good stability against aging. The sensing mechanism was explained based on established literature in which O_2^- ions in NHNP surface interacted with incoming ethanol molecules thereby releasing electrons back to the NHNP along with decomposition of ethanol into CO_2 as a gas. The presence of O_2^- ion in NHNP surface was confirmed by XPS whereas release of CO_2 was confirmed by FTIR spectroscopy. Thus, our work not only strongly establishes the potential use of NHNP as a low-cost and durable ethanol sensor that can detect ethanol from a mixture of humid air with high sensitivity and selectivity at room temperature but also experimentally verifies the sensing mechanism.

Acknowledgement:

PT acknowledges the University Grants Commission, Govt. of India for the fellowship award (UGC-JRF). AKC gratefully acknowledges the MHRD, Govt. of India for the Centre of Excellence (CoE) grant under TEQIP-III, May 2018 to NIT Durgapur.

References:

[1] J. Meng, J. Liu, Y. Xu, D. Guan, Z. Liu, Y. Huang, S. Tao, Proc. R. Soc. A: Math. Phys. Eng. Sci. 472 (2016) 20160380 (17 pp).

[2] Farid E. Ahmed, Crit. Rev. Toxicology 25(4) (1995) 347-367.

[3] K.M. Tripathi, T. Kim, D. Losic, T.T. Tung, Carbon N. Y. 110 (2016) 97–129.

[4] T.D.C. Minh, S.R. Oliver, J. Ngo, R. Flores, J. Midyett, S. Meinardi, M.K. Carlson, F.S. Rowland, D.R. Blake, P.R. Galassetti, Am. J. Physiol. Metab. 300 (2011) E1166–E1175.

[5] J.-J.Ho,Y.K. Fang, K.H. Wu, W.T. Hsieh, C.H. Chen, G.S. Chen, M.S. Ju, J.-J. Lin, S.B. Hwang, Sens. Actuators B: Chem. 50 (1998) 227–233.

[6] K. Warriner, A. Morrissey, J. Alderman, G. King, P. Treloar, P.M. Vadgama, Sens. Actuators B: Chem. 84 (2002) 200–207.

[7] F. Biasioli, F. Gasperi, C. Yeretzian, T.D. Märk, Trends Anal. Chem. 30 (2011) 968–977.

[8] S. G.Chatterjee, S. Chatterjee, A.K. Ray, A.K. Chakraborty, Sens. Actuators B: Chem. 221 (2015) 1170–1181.

[9] G. Jiménez-Cadena, J. Riu, F.X. Rius, Analyst. 132 (2007) 1083–1099.

[10] D.R. Miller, S.A. Akbar, P.A. Morris, Sens. Actuators B: Chem. 204 (2014) 250–272.

[11] Z. Lou, J. Deng, L. Wang, L. Wang, T. Fei, T. Zhang, Sens. Actuators B: Chem. 176 (2013) 323–329.

[12] N.G. Patel, P.D. Patel, V.S. Vaishnav, Sens. Actuators B: Chem. 96 (2003) 180–189.

[13] M. Sinha, R. Mahapatra, B. Mondal, R. Ghosh, J. Electron. Mater. 46 (2017) 2476–2482.

[14] P.Das, B. Mondal, K. Mukherjee, RSC Adv. 4 (2014)31879–31886.

[15] X. Chu, P. Dai, S. Liang, A. Bhattacharya, Y. Dong, M. Epifani, Phys. E 106 (2018) 326–333.

[16] S. G. Chatterjee, S Dey, D Samanta, S Santra, S Chatterjee, PK Guha, AK Chakraborty, J. Mater. Sci.: Mater. Electron. 29 (23) (2019) 20162-20171.

[17] X. Chu, J. Wang, L. Bai, Y. Dong, W. Sun, W. Zhang, Sens. Actuators B: Chem. 255 (2018) 2058–2065.

[18] A. Bhattacharya, Y. Jiang, Q. Gao, X. Chu, Y. Dong, S. Liang, A.K. Chakraborty, J. Mater. Res. 34 (2019) 2067–2077.

[19] T. Maekawa, J. Tamaki, N. Miura, N. Yamazoe, S. Matsushima, Sens. Actuators B: Chem. 9 (1992) 63–69.

[20] X. Q. Li, J. Q. Wei, J. C. Xu, H. X. Jin, D. F. Jin, X. L. Peng, B. Hong, J. Li, Y. T.Yang, H. L. Ge, X. Wang, J Nanopart. Res. 19 (2017), 396.

[21] S. Dey, S. Santra, S.K. Ray, P.K. Guha, IEEE Sensor J. 18(2018)15.

[22] C. Zhao, J. Fu, Z. Zhang, E. Xie, RSC Adv. 3(2013) 4018-4023.

[23] X. Chu, D. Jiang, Y. Guo, C. Zheng, Sens. Actuators B: Chem. 120 (2006) 177–181.

[24] X. Chu, C. Wang, D. Jiang, C. Zheng, Chem. Phys. Lett. 399 (2004) 461-464.

[25] L. Wang, Y.Kang, X. Liu, S. Zhang, W. Huang, S. Wang, Sens. Actuators B: Chem. 162 (2012) 237-243.

[26] E. Sennik, N. Kilinc, Z.Z. Ozturk, J. Alloys Comp. 616 (2014) 89–96.

[27] Y.-X. Li, Z. Guo, Y. Su, X.-B. Jin, X.-H. Tang, J.-R. Huang, X.-J. Huang, M.-Q. Li, J.-H. Liu, ACS Sensors. 2 (2017) 102–110.

[28] S. Wei, S. Wang, Y. Zhang, M. Zhou, Sens. Actuators B: Chem. 192 (2014) 480–487.

[29] W. Guo, T. Liu, H. Zhang, R. Sun, Y. Chen, W. Zeng, Z. Wang, Sens. Actuators B: Chem. 166–167 (2012) 492–499.

[30] A. Klini, S. Pissadakis, R.N. Das, E.P. Giannelis, S.H. Anastasiadis, and D. Anglos, J. Phys. Chem. C 119 (2015)623–631.

[31] P. Shankar and J.B.B. Rayappan, Sens. Lett. 11(2013)1956 .

[32] T. Kondo, Y. Sato, M. Kinoshita, P. Shankar, N.N. Mintcheva, M. Honda, S. Iwamori, and S.A. Kulinich, Jpn. J. Appl. Phys. 56(2017)080304.
[33] P. Shankar and J.B.B. Rayappan, J. Mater. Chem. C 5, 10869 (2017).
[34] P. Shankar and J.B.B. Rayappan, ACS Appl. Mater. Interfaces 9(2017) 38135.
[35] P. Tiwary, R. Mahapatra, A.K. Chakraborty, J. Mater. Sci. Mater. Electron. 30 (2019) 5464–5469.
[36] P. Tiwary, N. Chakrabarty, A.K. Chakraborty, R. Mahapatra, Materials Today: Proceedings 11 (2019), 875-878.
[37] T. P. Mokoena, H. C.Swart, D.E. Motaung, J. Alloys Comp. 805 (2019) 267-294.
[38] I. Hotovy, L. Spiess, M. Predanocy, V. Rehacek, J. Racko, Vaccum 107(2014), 129–131.
[39] S. Park, H. Kheel, G. Sun, S.K. Hyun, S.E. Park, Bull. Korean Chem. Soc., 37(2016), 713–719.
[40] X. Li, D. Li, J. Xu, H. Jin, D. Jin, X. Peng, B. Hong, J. Li, Y. Yang, H. Ge, X. Wang, Powder Technol. 318(2017), 40–45.
[41] Z. Yong, X. L.-Zhen, Li Hai-Rong, W. Peng, L. Su, P. Y.-Quan, Z. Miao, Chin.Phys.Lett. 32,(9) (2015) 098103.
[42] I. Chakraborty, N. Chakrabarty, A. Senapati, A.K. Chakraborty, J. Phys. Chem. C. 122 (2018) 27180-27190.
[43] N. Chakrabarty, A.K. Chakraborty, Electrochim. Acta. 297 (2019) 173–187.
[44] N. Chakrabarty, A.K. Chakraborty, H. Kumar, J. Phys. Chem. C. 123 (2019) 29104–29115.
[45] G. Zhu, H. Xu, Y. Liu, C. Xi, J. Yang, X. Shen, J. Zhu, J. Colloid Interface Sci. 412 (2013) 100–106.
[46] G. Zhu, Y. Liu, C. Xi, C. Bao, H. Xu, X. Shen, X. Zhu, Cryst. Eng. Comm. 15 (2013),9189–9195.
[47] G. Li, X. Wang, H. Ding, T. Zhang, RSC Adv. 2 (2012) 13018–13023.
[48] R.S. Mcewen, Crystallographic studies on Nickel Hydroxide and the higher Nickel Oxides,J. Phys. Chem. 75, (1971),1782–1789.
[49] A.Livingstone, D.L. Bish, On the new mineral theophrastite, a nickel hydroxide, from Unst, Shetland, Scotland., Mineralogical Magazine, 46(338),(1982),1-5
[50] S.M.D. Watson, K.S. Coleman, A.K. Chakraborty, ACS Nano 2 (2008) 643–650.
[51] S.P. Mondal, A. Dhar, S.K. Ray, A.K. Chakraborty, J. Appl. Phys. 105 (2009), 084309.
[52] J.J.Yeh, I. Lindau, Atomic Data and Nuclear Data Tables 32 (1985)1-55.
[53] M.C. Biesinger, B.P. Payne, L.W.M. Lau, A. Gerson, R.S.C. Smart, Surf. Interface Anal. 41 (2009) 324–332.
[54] S. Riseborough, J. Phys. Chem. Solids 52 (1991) 1397–1399.
[55] E.L. Ratcliff, J. Meyer, K.X. Steirer, A. Garcia, J.J. Berry, D.S. Ginley, D.C. Olson, A. Kahn, N.R. Armstrong, Chem. Mater. 23 (2011), 4988−5000.
[56] A. Bhattacharya, X. Chu, Q. Gao, X. Li, Y. Dong, S. Liang, and A. K. Chakraborty, Appl. Surf. Sci. 504 (2020), 144289.
[57] A. Bhattacharya, X. Chu, Y. Dong, S. Liang, A. K. Chakraborty, Vacuum 180 (2020), 109645.
[58] A. Adhikari, P. Tiwary, D. Rana , A Halder, J. Nath, A. Basu, D. Ghoshal, P. Kar , A. K. Chakraborty, D. Chattopadhyay, J. Environm. Chem. Engg. 8 (2020)104249.
[59] M. J. Eslamibudgoli, A Gross, M. Eikerling, Phys. Chem. Chem. Phys. 19 (2017) 22659.
[60] J. Cheng, M.A. Rasheed, K.M. Poduska, ECS J. Solid State Sci. Technol. 2 (1) (2013),Q23-Q26.

[61] C. M. Owens, J.M. Roscoe, Can. J. Chem. 54(1976), 984-989.
[62] A. Kato, R.J. Cvetanovic, Can. J. Chem. 46 (1968) 235-250.
[63] Y. Seekaew, A. Wisitsoraat, D. Phokharatkul, C.Wongchoosuk, Sens. Actuators B: Chem. 279 (2019) 69–78.
[64] P. Yang, X. Ye, C. Lau, Z. Li, X. Liu, J. Lu, Anal. Chem. 79 (2007) 1425–1432.
[65] A. Umar, F. Al-hazmi, G. N. Dar, S. A. Zaidi, R.M. Al-tuwirqi, F. Alnowaiserb, A.A. Al-ghamdi, S.W. Hwang, Sens. Actuators B: Chem. 166–167 (2012) 97–102.
[66] A. Dąbrowski, Adv. Colloid Interface Sci. *93* (2001) 135–224.
[67] R. De Gryse, W. P. Gomes, F. Cardon, and J. Vennik, J. Electrochem. Soc. 122 (1975) 711.
[68] R. Acharya, T. Subbaiah, S. Anand, R.P. Das, J. Power Sources, 109 (2002) 494–499.
[69] P. Baraldi, G. Davolio , G. Fabbri, T. Manfredini, Mater. Chem. Phys., 21 (1989), 479-493.